

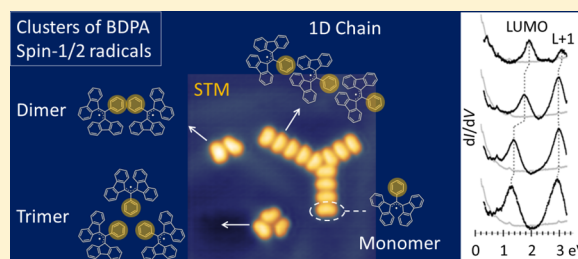
## Interactions and Self-Assembly of Stable Hydrocarbon Radicals on a Metal Support

Stefan Müllegger,\* Mohammad Rashidi, Michael Fattinger, and Reinhold Koch

Institute of Semiconductor and Solid State Physics, Johannes Kepler University Linz, 4040 Linz, Austria

## Supporting Information

**ABSTRACT:** Stable hydrocarbon radicals are able to withstand ambient conditions. Their combination with a supporting surface is a promising route toward novel functionalities or carbon-based magnetic systems. This will remain elusive until the interplay of radical–radical interactions and interface effects is fundamentally explored. We employ the tip of a low-temperature scanning tunneling microscope as a local probe in combination with density functional theory calculations to investigate with atomic precision the electronic and geometric effects of a weakly interacting metal support on an archetypal hydrocarbon radical model system, i.e., the exceptionally stable spin-1/2 radical  $\alpha,\gamma$ -bisdiphenylene- $\beta$ -phenylallyl (BDPA). Our study demonstrates the self-assembly of stable and regular one- and two-dimensional radical clusters on the Au(111) surface. Different types of geometric configurations are found to result from the interplay between the highly anisotropic radical–radical interactions and interface effects. We investigate the interaction mechanisms underlying the self-assembly processes and utilize the different configurations as a geometric design parameter to demonstrate energy shifts of up to 0.6 eV of the radicals' frontier molecular orbitals responsible for their electronic, magnetic, and chemical properties.



## INTRODUCTION

Free radicals (i.e., molecules with one or more unpaired electrons) are ubiquitous in living systems<sup>1</sup> as well as engineered synthetic routes.<sup>2</sup> The number of stable radicals is comparatively small,<sup>3</sup> because of the peculiar requirements for stabilizing the unpaired electron state against reaction with its atomic surroundings, which has fascinated scientists ever since the first observations by Gomberg.<sup>4,5</sup> Once prepared, stable free radicals can be stored and investigated under ambient conditions and thus are desirable spin standards, polarizing agents,<sup>6</sup> and building blocks of molecule-<sup>7</sup> or carbon-based<sup>8</sup> magnetic systems. In recent years, purely hydrocarbon stable free radicals (like phenalenyl<sup>9</sup>) turned out to be suitable model systems for investigating  $sp^2$  magnetism<sup>7,10</sup> in reduced dimensions—along with other benzenoid compounds like graphene flakes,<sup>11</sup> carbon nanotubes,<sup>12</sup> fullerenes,<sup>13</sup> and  $\pi$ -conjugated polymers.<sup>14</sup>

An important goal in this context is obtaining a fundamental understanding of how stable radicals interact with each other.<sup>3,9,15,16</sup> To date, however, a comprehensive fundamental understanding of interactions between stable radicals still remains elusive. One problem is that the possible types of interactions between radicals are manifold, often resulting in a complex competition between various types.<sup>9,15</sup> Second, most systems were so far studied in liquid phase, making it difficult to track individual radicals and to investigate their interaction with surrounding radicals at the atomic scale.

Our study contributes to the fundamental understanding of radical–radical interaction by demonstrating insight into the

electronic properties of interacting radicals at the single-radical level. We have investigated how the self-assembly on a weakly interacting metal support affects the frontier-orbital electronic structure responsible for the desired radical properties. To avoid complex metal–organic bond formation, we have chosen an exceptionally stable and purely hydrocarbon radical, the “Koelsch radical”,<sup>18</sup>  $\alpha,\gamma$ -bisdiphenylene- $\beta$ -phenylallyl (BDPA,  $C_{33}H_{22}$ ), which is a well-known stable spin-1/2 complex<sup>19,20</sup> (Figure 1a). We observe self-assembly of regular radical clusters with different geometric properties—either one-dimensional chains or 3-fold symmetric trimers or 2-fold symmetric dimers—steered by the substrate atomic lattice. The geometric properties reveal a strong anisotropy of the radical–radical interaction and affect the energies of the frontier molecular orbitals (MOs) by up to 0.6 eV.

## METHODS

BDPA recrystallized in benzene was thermally evaporated in ultrahigh vacuum (UHV) from a quartz crucible at 383 K after thorough degassing at 373 K. The single-crystal Au(111) surface was prepared by repeated cycles of 0.5 keV  $Ar^+$  bombardment and annealing at 720 K. STM and STS experiments were carried out at 7 K employing electrochemically etched W tips deoxidized by annealing in UHV. The  $dI/dV$  signal was obtained from the first-harmonic current signal

Received: July 10, 2012

Revised: September 3, 2012

Published: October 4, 2012

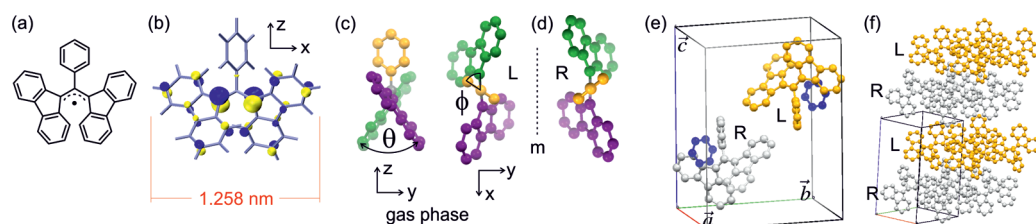


**Figure 1.** Structure details of the BDPA radical. (a) Chemical structure. (b–d) DFT results of BDPA in the gas phase. (b) Isodensity surface representation of the SOMO of BDPA; the cutoff value is  $0.055 e/a_0^3$ , where  $e$  is the elementary (negative) charge of the electron and  $a_0$  is the Bohr radius; blue/yellow indicates an opposite sign of the wave function. (c) Side-view and top-view of left-handed (L) stereoisomer;  $\theta$  and  $\phi$  denote dihedral and torsion angle. (d) Top-view of the right-handed (R) stereoisomer. (e, f) Crystalline bulk structure of BDPA:benzene (from ref 17). (e) Monoclinic unit cell containing both L (orange) and R (gray) stereoisomers; benzene is blue; the parameters of the monoclinic bulk unit cell are  $a = 0.95$  nm,  $b = 1.46$  nm,  $c = 1.95$  nm, and  $\beta = 93.6^\circ$ . (f) Alternating layers of L and R isomers.

detected by lock-in technique (0.5–2 kHz; 5–20 mV sinusoidal peak-to-peak voltage; average of 3–10 single spectra). Impurity and tip effects were minimized by careful sample preparation and multiple tip formings between the dI/dV experiments. Reliable tip performance was established by accurately reproducing the dI/dV signature of the Au(111) surface state from the literature.<sup>21</sup> dI/dV spectra were recorded under both constant-height and constant-current conditions. The latter has allowed the bias-voltage range to be extended to higher values in the empty-states regime without disturbing or exciting the BDPA radical in the tunnel junction. Note that constant-current spectroscopy leads to point contact when the bias voltage approaches zero, causing a rapid increase of the background conductance signal at small bias voltages.

Spectroscopic images (dI/dV maps) were recorded simultaneously during constant-current topographic imaging. The dI/dV maps of surface-supported molecules image the wave function  $|\Psi(x,y)|^2$  of a particular MO selectable by the bias voltage. In contrast to the case of, e.g., electronic bands of a pristine metal surface, the spectroscopic signal from the adsorbed radicals may not be misinterpreted as the local density of states (DOS). The adsorbed radicals preserve their (discrete) MOs upon adsorption on the weakly interacting surface, and each MO exhibits a “constant DOS” equal to 1. Rather than the local DOS, a dI/dV map of a molecule images the spatial electron distribution within the selected MO over the molecular backbone.

Gas-phase density functional theory (DFT) single point energy calculations were performed with the Gaussian 03 package<sup>22</sup> using the B3LYP hybrid functional,<sup>23</sup> 6-31G(d) basis set. Although the predictive quality of DFT-calculated MO energies is generally poor,<sup>24,25</sup> the symmetry and spatial extent of MOs typically are reliable and hence useful for interpreting our experimental data.

## RESULTS AND DISCUSSION

**BDPA Radical.** BDPA is a sterically protected spin-1/2 hydrocarbon radical. An unpaired  $\pi$  electron is stabilized by delocalization over the radical backbone<sup>17</sup> in the singly occupied (highest) molecular orbital (SOMO) (Figure 1b), as calculated by DFT. Early X-ray diffraction studies found an approximate  $C_2$  symmetry of the BDPA monomer in the bulk phase<sup>17</sup>—consistent with our DFT results for gas-phase BDPA (Figure 1c). Each of the two fluorenyl units is almost planar and tilted by a dihedral angle  $\theta$  with respect to the other (plotted in green and purple in Figure 1c). In the crystalline bulk phase<sup>17</sup> of BDPA:benzene and BDPA:acetone, the dihedral angle was found to be  $\theta = 60^\circ$ .<sup>17</sup> In the gas phase, it

increases to  $\theta \approx 64^\circ$  (see DFT results of Figure 1c). An even larger value of  $\theta \approx 74^\circ$  has been suggested in toluene solution.<sup>26</sup>

The phenyl unit of BDPA (plotted in orange in Figure 1c) is twisted by the torsion angle  $\phi \approx \pm 51^\circ$ , giving rise to stereoisomers denoted as left-handed (L) and right-handed (R) (Figure 1c and d). Indeed, both L and R stereoisomers are contained in the crystalline unit cell of BDPA:benzene<sup>17</sup> (Figure 1e) and the respective bulk phase exhibits alternating layers of L and R stereoisomers (Figure 1f).

In the bulk phase, BDPA possesses a nearly isotropic  $g$ -factor of  $g = 2.0026$  at room temperature and  $g \approx 2.008$  at 4 K.<sup>27</sup> Our electron paramagnetic resonance (EPR) experiments in the X band on samples with BDPA monolayer coverage adsorbed on Au(111)/mica substrates yield a value of  $g = 1.96$  at 7 K, which is in good agreement with the above low-temperature value of the bulk phase. The observed EPR activity of BDPA/Au(111) together with the small  $g$ -shift of about 2% compared to the bulk indicate that the BDPA radicals adsorbed on the Au(111) surface preserve the radical spin-1/2 state and, furthermore, suggest that a possible charge transfer from the Au substrate is small.

**Radical-Cluster Geometries.** We have prepared ultrathin BDPA films on a single-crystal Au(111) substrate by vacuum sublimation. The Au(111) surface is reconstructed, forming the well-known zigzag “herringbone” pattern<sup>28,29</sup> of (two out of three) alternating  $120^\circ$  rotational domains (Figure 2a). Each domain exhibits equidistant pairs of parallel corrugation lines (0.02 nm high) that separate fcc and hcp stacked regions of the surface atomic lattice. At each domain boundary, the corrugation lines are kinked, giving rise to the characteristic zigzag pattern. The kinks of one of the two lines exhibit a characteristic surface lattice dislocation, leading to the formation of bulged and pinched “elbow” sites<sup>30</sup> marked by arrows in Figure 2a. These sites are preferential pinning centers for a number of molecular adsorbates.<sup>31</sup>

We have studied samples, prepared at 300 and 130 K, with STM. The nominal thickness of the BDPA films was varied from submonolayer coverage up to a full monolayer. Figure 2b shows an STM topographic overview image of the sample surface after deposition of 0.2 monolayers of BDPA at 300 K. The atomic lattice of the substrate appears to be undisturbed by the adsorbed radicals and the Au(111) herringbone reconstruction is preserved, evidencing weak physisorption of BDPA on Au(111). Multiple BDPA monomers agglomerate and form clusters by self-assembly, indicating a rather high surface mobility of the single monomer at 300 K. Literally, no isolated monomers are observed on the 300 K sample, but a few can be

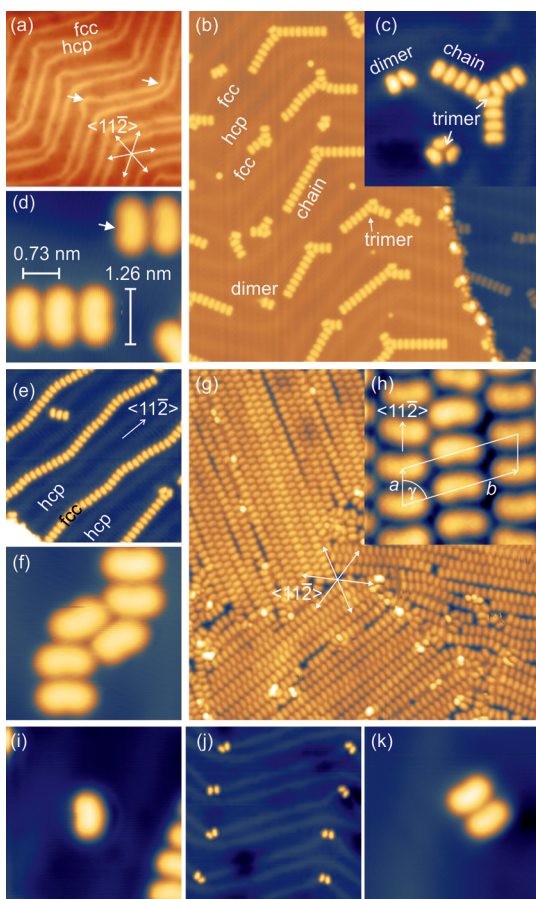


**Figure 2.** STM topographic images of BDPA on Au(111) at +1 V showing the structural diversity of different BDPA clusters. (a) Herringbone reconstruction of the pristine Au(111) surface;  $36 \times 36 \text{ nm}^2$ ; arrows mark elbow sites (see text). (b) 0.2 monolayers of BDPA grown at 300 K;  $40 \times 40 \text{ nm}^2$ . (c) Close-up image ( $10 \times 10 \text{ nm}^2$ ) of characteristic self-assembled BDPA clusters denoted as dimer, trimer, and chain. (d) Bean-shape appearance of BDPA monomers; the arrow marks the concave side of the topographic bean-shape of the BDPA monomer (see text); scale-bars indicate the radical–radical separation and monomer length. (e) One-dimensional BDPA chains grown on fcc regions. (f) Typical structure of an irregular BDPA cluster on the 130 K sample;  $4 \times 4 \text{ nm}^2$ . (g) Full monolayer;  $60 \times 60 \text{ nm}^2$ . (h) Local quasicrystalline order of a full BDPA monolayer; the two-dimensional unit cell is indicated. (i) Isolated monomer. (j) Dimer formation at elbow sites at low submonolayer coverage of only 0.05 monolayers. (k)  $N = 2$  chain; here the monomers are aligned parallel, in contrast to the dimer.

found on the 130 K sample (Figure 2i). We have found a number of different cluster types distinguished by geometry (separation and orientation of monomers). We denote them as chain, trimer, and dimer, as shown in Figure 2c and discussed in detail below. The cluster types serve as model systems for investigating geometry effects on the radical–radical interaction.

At substrate temperatures of 300 and 130 K, the BDPA radicals predominantly form directed one-dimensional chains on the Au(111) surface (Figure 2b). Individual BDPA radicals are imaged by STM as protrusions with a characteristically curved contour (“bean-shape”) best seen in Figure 2d. The concave side of the bean-shape (marked by an arrow) points in the direction of a growing chain. The nominal length of 1.26 nm of the BDPA monomer derived from the structure model of

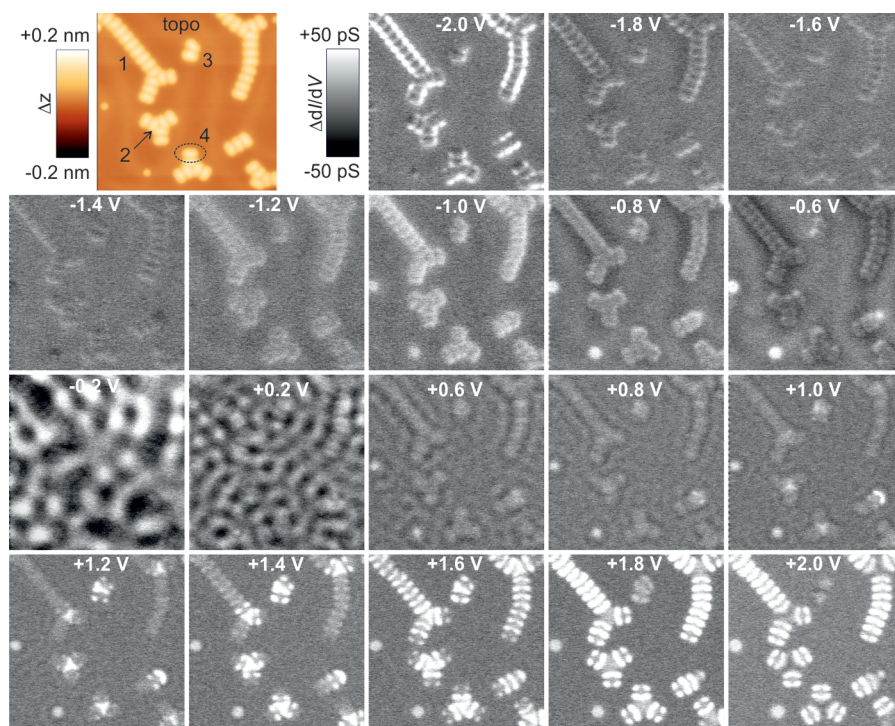
Figure 1b is indicated by a vertical bar. Within the chains, the radicals are regularly aligned at a separation of  $0.73 \pm 0.05 \text{ nm}$  (center-to-center). This value is significantly smaller than that in similar chains found in the bulk structure and the full monolayer (see below). (In the bulk crystal structure, linear chains of homoenantiomeric BDPA radicals run along the  $\vec{a}$  and  $\vec{b}$  crystallographic directions, with uniform radical–radical separations of 0.95 and 1.47 nm, respectively (see Figure 2e).) At low coverage, BDPA chains grow preferentially on fcc regions (which exhibit a lower surface electron density of states compared to hcp regions<sup>32</sup>) and follow the herringbone pattern along two out of three symmetry-equivalent  $\langle 11\bar{2} \rangle$  directions, i.e., approximately parallel to the corrugation lines of the reconstructed Au(111) surface (see Figure 2e). A detailed analysis of the bean shapes of individual radicals in the STM topographs reveals that all BDPAs in a chain exhibit the same azimuthal orientation (see Figure 2d,h).

Chain growth at 300 K typically starts from nucleation centers consisting of an ordered cluster of three BDPAs arranged in an almost 3-fold symmetric manner over fcc regions (Figure 2b,c). We denote them as trimers. Their radical–radical separation varies between 0.85 and 0.95 nm, which is significantly wider than in the chain. At a growth temperature of 130 K, regular trimers are rare and nonregular clusters similar to that shown in Figure 2f act as nucleation centers for chains instead.

Up to coverages of a full monolayer, the chains dominate. They overgrow both fcc and hcp regions, packing almost parallel with a chain–chain separation of about 1.20 nm and forming approximate  $120^\circ$  rotational domains (Figure 2g). The azimuthal alignment of the chains indicates a guidance of the one-dimensional BDPA chains by the underlying Au(111) substrate. Locally, a two-dimensional quasi-crystalline order is established in the monolayer, where the azimuthal orientation of neighboring chains alternates regularly (Figure 2h). The respective two-dimensional unit cell is illustrated in Figure 2h with cell parameters  $\vec{a} = 0.84 \text{ nm}$ ,  $\vec{b} = 2.6 \text{ nm}$ , and  $\gamma = 71 \pm 2^\circ$ . Compared to submonolayer coverages, the radical–radical separation along the chain is increased by 15% in the full monolayer. This reduced packing density along the chains suggests a suppression of inter-radical attraction of neighboring-chain BDPAs.

For small submonolayer coverages (e.g., below 0.1 monolayers) at 300 K, we find dimers of BDPA rather than chains. The dimers are preferentially located at elbow sites (Figure 2j), and the individual BDPAs are oriented with their concave sides (bean shape) pointing away from each other in a characteristic V-like manner (Figure 2c). The radical configuration in dimers differs from that in chains with  $N = 2$  radicals (Figure 2k), which form over fcc regions instead of elbow sites and exhibit no V-shape. The V-shape of dimers seems to be caused by a slight tilting of the radicals upon adsorption on the anisotropically corrugated atomic lattice<sup>33</sup> of the elbow sites. This leads to an increased radical–radical separation of  $0.80 \pm 0.05 \text{ nm}$  in dimers that is larger than in chains but smaller than in trimers. With increasing coverage, dimers are used up by the formation of more and more chains. On samples grown at 130 K, dimers are rarely observed independent of coverage.

**Geometry Effects on the Frontier Orbitals.** We found that the different cluster geometries of chain, trimer, and dimer affect the energies of the frontier MOs detected by spectroscopic imaging and point spectroscopy (see Methods).



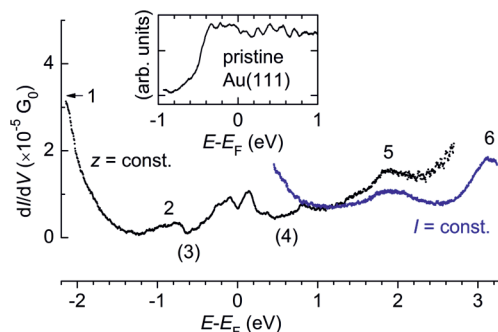
**Figure 3.**  $dI/dV$  spectroscopic images of different BDPA cluster types on Au(111) recorded at different sample bias voltages; chain, trimer, dimer, and monomer (see text) are labeled 1–4.

Figure 3 shows a series of spectroscopic images ( $dI/dV$  maps) recorded at different bias voltages in constant-current mode. Each frame shows the same sample area, including BDPA chain, trimer, and dimer (labeled 1–3, respectively). The terminating (outermost) monomer of clusters like that labeled 4 in Figure 3 is found to behave like an isolated monomer. At certain bias voltages, the BDPA radicals are imaged as bright protrusions (increased conductance), indicating resonant tunneling across certain occupied and empty MOs. The shape of the protrusions varies strongly and takes on characteristic forms around  $-2$ ,  $-1$ , and  $+2$  V. In contrast, BDPA is hardly visible at  $-1.4$ ,  $-0.2$ , and  $+0.2$  V against the conductance background of the pristine Au(111) surface, suggesting that these energies lie between those of radical MOs.

A detailed analysis of Figure 3 reveals that each type of cluster has its own characteristic resonance energy that differs by up to  $0.6$  eV among different cluster types (see discussion below). This is best seen in the empty-states regime (positive sample bias) of Figure 3. Around  $+1.2$  V, dimers and trimers are clearly in resonance (enhanced conductance), while chains and monomers are hardly visible (off resonance). The situation is reversed at a higher energy of  $+1.8$  to  $+2$  V, where chains are in resonance and dimers and trimers are off-resonance. Obviously, the geometric properties of the clusters affect the frontier-orbital electronic structure of the involved radicals. The cluster size (chain length  $N$ ; even or odd) has no significant effect. In the following, we elucidate the geometry effect with point spectroscopy and spectroscopic imaging at the single-radical level.

**Point Spectroscopy of the One-Dimensional BDPA Chain.** We have determined by point spectroscopy all the observable frontier MOs of BDPA within an energy range of a few eV around the substrate Fermi level. The best results (highest reproducibility) are obtained for the case of the BDPA chain, which we found to be the structurally best-defined cluster

type. Figure 4 shows representative local  $dI/dV$  spectra of a chain recorded at constant-height (black curve) and constant-



**Figure 4.**  $dI/dV$  point spectra of a surface-supported BDPA chain recorded under constant-height (black) and constant-current (blue) conditions with the STM tip over BDPA. Inset: spectrum of the pristine Au(111) substrate.

current (blue) conditions. (The high surface mobility of BDPA causes motional instability of BDPA in the STM tunnel junction, restricting our constant-height spectroscopy experiments to an energy range of about  $-2$  to  $+2.7$  eV. Thus, we added constant-current spectra (blue) in Figure 4, which allowed the energy range to be extended above  $+3$  V. Note that energy differences of a few tenths of electronvolts between constant-height and constant-current spectra are not unusual and are often due to  $z$ -effects.<sup>34</sup>) Typical spectra exhibit a strong filled-state resonance below  $-2$  V (labeled resonance 1) together with a weak broad resonance spanning from  $-1.1$  to  $-0.7$  eV (resonance 2) and two strong features at  $+1.9$  eV (resonance 5) and  $+3.1$  eV (resonance 6) in the empty-states regime. We assign these resonances to the highest doubly occupied and lowest doubly unoccupied MOs—in agreement

with our DFT results (see discussion below). The feature at zero bias is due to vibrational excitations and the Kondo effect and will be discussed in detail elsewhere.<sup>35</sup> No distinct SOMO/SUMO resonances are observed in the spectra of Figure 4, neither in constant-current mode nor in constant-height mode. We remark that, because of the large Coulomb interaction, these orbitals are replaced by broad Hubbard bands, generally not prominent in STS. Nevertheless, we have inferred approximate positions of SOMO/SUMO from comparison with the conductance background of the pristine Au surface based on the  $dI/dV$  maps of Figure 3 as described in section S1 of the Supporting Information. The SOMO/SUMO signals are weak, and the respective energies are marked by (3) and (4) in Figure 4. The complete peak assignment is listed in Table 1.

**Table 1. Energies of  $dI/dV$  Resonances in eV Obtained by Point Spectroscopy at Constant  $z$  and Constant  $I$  of BDPA Radicals in Linear Chains Adsorbed on Au(111)**

resonance	energy ( $\pm 0.2$ eV)	assignment
1	$< -2$	HOMO-1
2	$-1.1$ to $-0.75$	HOMO
3	$\approx -0.6$	SOMO
4	$\approx +0.6$	SUMO
5	$+1.9$	LUMO
6	$+3.1$	LUMO+1, +2

The small feature at  $+0.8$  eV in the constant-height curve of Figure 4 most likely belongs to the broad SUMO resonance, starting at  $+0.6$  eV (see section S1 of the Supporting Information).

#### Point Spectroscopy of Different BDPA Cluster Types.

We have determined the characteristic resonance energies of different cluster types by point spectroscopy. We focus on the empty-states regime (LUMO and LUMO+1), where the energy shift is found to be considerably stronger compared to the filled frontier-orbital state. Figure 5b shows a compilation of  $dI/dV$  spectra for the monomer, chain, dimer, and trimer (black curves) plotted against the spectrum of the pristine Au(111)

surface (gray curves). The conductance resonances 5 and 6 are observed for all cluster types, but the resonance energies vary depending on the cluster type. Table 2 lists the observed

**Table 2. Energies in eV of MO Resonances 5 and 6 of Different Types of BDPA Clusters (Monomer, Chain, Dimer, Trimer) and Energy Shifts in eV Relative to the Adsorbed Monomer<sup>a</sup>**

	resonance 5		resonance 6	
	energy	shift	energy	shift
monomer	+1.90		+3.07	
chain	+1.76	−0.14	+3.00	−0.07
dimer	+1.35	−0.55	+2.98	−0.09
trimer	+1.28	−0.62	+2.90	−0.17

<sup>a</sup>The data were obtained from the constant-current spectra of Figure 5b.

resonance energies together with the energy shift relative to the isolated monomer. The strongest shift of  $-0.62$  eV is observed for resonance 5 (LUMO) of the trimer.

**$dI/dV$  Mapping of Frontier MOs.** We determined the spatial properties of the energy-shifted frontier MOs by spectroscopic imaging. Respective maps of the LUMO-related  $dI/dV$  resonance 5 are shown in Figure 5c. The topmost map shows the characteristic (low-symmetry) shape of resonance 5 of the single monomer. With this fingerprint of the monomer, it is possible to “decode” all other  $dI/dV$  maps of Figure 5c, including those of the chain, dimer, and trimer. The apparently more complex maps of all the structurally different clusters observed in our study are found to be (linear) superpositions of multiple monomer fingerprints. This is best seen by comparing the experimental maps with the red, black, and blue sketches illustrated at the right side of each conductance map in Figure 5c. The sketches are guides to the eye that facilitate recognizing this “superposition principle”. Analyzing the LUMO+1-related resonance 6 yields a similar result (see Figure 5d). (In the case of the single monomer, it was not possible to record the  $dI/dV$  map of resonance 6, because of excitation of lateral motion by

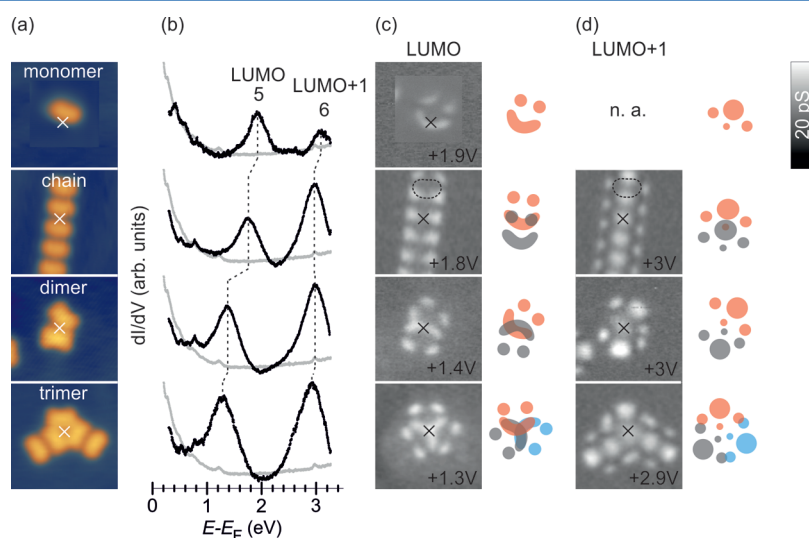


**Figure 5.** Lowest unoccupied MOs of BDPA in different cluster types (monomer, chain, dimer, trimer). (a) STM topographs at  $+1$  V;  $\times$  marks the STM tip position for spectroscopy. (b) Point spectra; the gray curve is pristine Au substrate between BDPA clusters. (c, d)  $dI/dV$  images of LUMO (resonance 5) and LUMO+1 (resonance 6); the dashed contour line indicates the position and size of the BDPA radical; red, black, and blue sketches beside each map are guides to the eye.

the STM tip.) A detailed analysis of the spectroscopic maps reveals considerable spatial overlap of the LUMO-related resonance 5 between neighboring radicals (compare sketches of Figure 5c for different cluster types). The different azimuthal orientations and lateral separations of individual BDPA in the dimer and trimer facilitate an even stronger overlap as compared to the chain. The amount of overlap depends on the type of cluster and scales almost linearly with the energy shift of the respective MO resonance. In contrast, the spatial shape of resonance 6 avoids strong overlap among neighboring BDPA in any type of cluster (see sketches of Figure 5d). Accordingly, the energy shift of resonance 6 in different cluster types is much smaller (Table 2).

#### Single-Radical Electronic and Geometric Properties.

On the basis of our combined STM and DFT results, we have determined a number of fundamental electronic and geometric properties of BDPA/Au(111) at the single-radical level. The apparent height of BDPA slightly depends on bias voltage and cluster type. For chains, it is 0.10–0.13 nm for bias voltages of  $\pm 1$  V, i.e., significantly smaller than the nominal width of a BDPA radical (see Figure 1b). Thus, an upright standing orientation (phenyl pointing perpendicular away from substrate) is unlikely. The topographic shape and symmetry of BDPA monomers (bean-shape) observed by STM indicates an inclined orientation of the monomers relative to the substrate plane, where the phenyl axis lies almost parallel to the substrate plane (see illustration of Figure 6d). We remark that such a

“flat-on” orientation requires an increase of the dihedral angle of the fluorenyls to more than  $90^\circ$ . Otherwise, a molecule–molecule separation as close as 0.73 nm determined by STM is sterically forbidden.

The assignment of MO resonances derived from our experimental STS data (Figure 4) and listed in Table 1 is qualitatively corroborated by a comparison with the DFT-calculated MO energies of the monomer in the gas phase (Figure 6a). (The predictive quality of the calculated absolute energy values is limited, since the Au substrate was not included in our calculations.) Figure 6b shows sketches (gray) of the shape and symmetry of the experimental  $dI/dV$  maps of resonances 5 and 6 (LUMO and LUMO+1) of the monomer determined from Figure 5. The topographic contour of the monomer is shown as a red line. For both resonances, the experimental  $dI/dV$  signal is weak if the STM tip is over BDPA and strong at certain positions near the rim of the radical. Most possibly, this is caused by the overlap with the STM tip wave function, which is weak over inner regions of the BDPA due to steric hindrance. The two conductance patterns of Figure 6b are almost complementary to each other. At the convex side of the bean-shape, the  $dI/dV$  signal is strong for resonance 5 but weak for resonance 6 (marked by arrows in Figure 6b). A detailed comparison with the DFT-calculated MO representations of Figure 6a reveals that both LUMO+1 (MO 112) and LUMO+2 (MO 113), which relate to the experimental resonance 6, are expected to have small electron density over the phenyl unit—similar to the convex side of resonance 6. (The electron density is proportional to the squared wave function of the respective MO,  $|\Psi_{\text{MO}}|^2$ .) We conclude that the convex side of the bean-shape STM topograph of the BDPA monomer coincides with the position of the phenyl. With this, it is finally possible to overlay a structure model over our experimental STM topographs in proper scale and orientation, as illustrated in Figure 6c for the full BDPA monolayer, one-dimensional chain, dimer, and trimer.

**Radical–Radical Interaction.** The preferred growth of one-dimensional (nondendritic) chains indicates a unidirectional attraction of neighboring radicals. BDPA is a nonpolar radical,<sup>6</sup> without functional (polar) groups to form strong directional bonds with neighboring radicals. The unidirectionality (spatial anisotropy) of the interaction can be explained by the stereochemical (geometric) shape of the radicals shown in the structure model of Figure 1c. The anisotropy indicates a preference for aligning fluorenyl units of neighboring radicals with their  $\pi$ -planes parallel to each other—similar to the  $\pi$ -stacking observed for many planar  $\pi$ -conjugated molecular compounds. This alignment facilitates the packing of the radicals at a regular separation as small as 0.73 nm along the chain observed by STM. On the basis of our findings, we propose a model structure of the BDPA chain on Au(111), as shown in Figure 6d. The model chain is illustrated as a homochiral domain similar to the linear chains of the bulk structure. The radicals are oriented in a side-on position with their phenyls pointing toward the central C atom of the next-neighbor radical (phenyl axis parallel to substrate plane).

The observed preferential growth of BDPA chains on fcc regions of the Au substrate may suggest the existence of a small negative partial charge on the adsorbed BDPA radicals (they are repelled by hcp regions with higher surface electron density). Recent studies of planar  $\pi$ -conjugated molecules adsorbed on atomically clean single-crystal coinage metal surfaces argue that the observation of a 1D growth mode

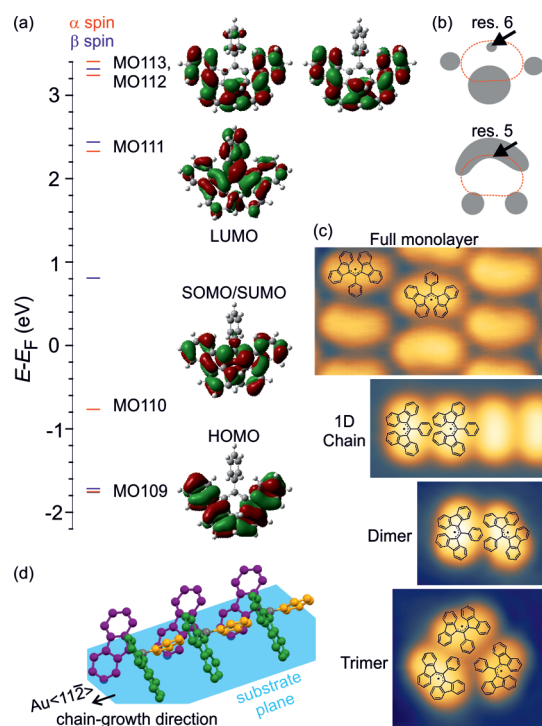


**Figure 6.** (a) DFT-calculated BDPA frontier MOs and energies in the gas phase; the SOMO/SUMO gap was arbitrarily chosen to be symmetric about the substrate Fermi level  $E_F$ . (b) Sketches of experimental  $dI/dV$  maps of resonances 5 and 6 of the BDPA monomer; the red line indicates the bean-shape topographic contour and position of the BDPA monomer; arrows mark the convex side of the bean-shape. (c) STM topographs with overlaid molecular structure of the individual BDPA radicals for the full monolayer, one-dimensional chain, dimer and trimer. (d) Model structure of a one-dimensional BDPA chain on Au(111).

(1D chain formation similar to that reported in the present study) would indicate a partial charge transfer, resulting from an interplay of short-range van der Waals attraction and long-range electrostatic repulsion.<sup>36</sup> A possible partial charge transfer is expected to result in an enhanced scattering in the two-dimensional electron gas of the Au(111) surface state at the charged adsorbate, which is clearly absent for BDPA/Au(111) (see  $dI/dV$  maps of Figure 3 at  $\pm 0.2$  V). Electrostatic effects seem to be small—in accordance with our EPR and STS results (see section S1 in the Supporting Information)—and thus of negligible relevance for the formation of the one-dimensional BDPA chains on Au(111).

The fluorenyl units exhibit a total  $\alpha$  (up) spin density, while a negative spin density ( $\beta$  spin) dominates on the phenyl group.<sup>17</sup> Our DFT results predict that increasing the dihedral angle  $\theta$  of the fluorenyls, anticipated for the chain, further increases the  $\beta$  spin density on the phenyl group, while the fluorenyls keep a total  $\alpha$  (up) spin density. The proposed model structure of the chain (Figure 6d) would thus be consistent with McConnell's picture<sup>10</sup> of ferromagnetic order based on the concept of intramolecular spin polarization. However, the  $\pi$ -stacked fluorenyls of the next-neighbor radicals in the model structure are separated by more than 5.5 Å. This is significantly larger than the  $\pi$ -stacking separation found in planar hydrocarbon radicals ( $\approx 3$  Å), for which recent studies revealed a combination of strong SOMO–SOMO overlap with dispersion forces giving rise to the so-called multicenter bonding configuration.<sup>9,37–39</sup> Thus, a direct magnetic interaction (overlap) is unlikely to contribute to the attractive interaction of radicals in the self-assembled BDPA chains on Au(111).

The topographic bean-shape of the monomer is unaffected by the type of cluster, indicating a predominantly noncovalent character of the radical–radical interaction. This interpretation is corroborated by the observed superposition principle, where the conductance pattern of the independent monomer is preserved for each MO resonance in the clusters (Figure 5c,d).

The interaction strength can be estimated from our sample preparation parameters [adsorption rate of  $2.6 \times 10^{11}$  radicals/(s·cm<sup>2</sup>) at 383 K source temperature; the surface coverage of the saturated monolayer  $\theta_0 = 9.4 \times 10^{13}$  radicals/cm<sup>2</sup> was obtained from the surface unit cell parameters above]. Assuming  $R_{\text{adsorption}} = R_{\text{desorption}}$  and using Redhead's equation<sup>40</sup> for zero-order thermal desorption,  $R = \nu_0 \theta_0 \exp(-E_{\text{des}}/(k_B T))$ , with  $\nu_0 \approx 10^{13}$ , we obtain an approximate value of  $E_{\text{des}} = 1.15$  eV per radical for the multilayer desorption energy of BDPA. This is a typical value for a van der Waals molecular compound<sup>41</sup> and should represent the upper limit for the attractive interaction between neighboring BDPA radicals in the chain. (Note that in the chain there are fewer next neighbor radicals that may attract each other compared to the crystalline bulk phase.)

Different substrate regions, like elbows or fcc regions, lead to the formation of different types of radical clusters, where the contained monomers have characteristic separations and orientations relative to their neighbor radicals. The structural variations among different cluster types provide a handle for studying geometry effects on the radical–radical interaction at the single-molecule level. We have determined the effect on the frontier MO energies (see Figure 5 and Table 2). Most likely, different contributions add up for the observed energy shift: (i) Sub-Angstrom changes of conformation and/or orientation of the radicals within different cluster types induced by the

anisotropic atomic lattice of the substrate. Similarly large energy shifts found in surface-supported porphyrins on Au(111) were recently attributed to conformational effects.<sup>33</sup> (ii) Variations of the tunneling distance during the recording of constant-current spectra. This is a natural consequence of (i). Similar “apparent” energy shifts are inherent of the STS method.<sup>34</sup> While the latter is a mere instrument effect, the former is a direct consequence of the radical–radical interaction. (iii) Contributions of van der Waals interaction.

The observed magnitude of MO-energy shifts for different cluster types can be explained with the help of our DFT results. For HOMO, LUMO, and LUMO+1, we have found minimum, maximum, and medium energy shift (see also Table 2 and Figure 5b). The magnitudes of the DFT-calculated electron density of these MOs over the phenyl ligand (see Figure 6a) follow a similar trend: HOMO has negligible, LUMO strongest, and LUMO+1 medium electron density among these three MOs at the phenyl position. A comparison with the structure models of Figure 6c indicates an enhanced phenyl–phenyl interaction between neighboring BDPA's for the dimer and trimer compared to the chain due to a significantly shorter phenyl–phenyl separation. Most likely, van der Waals or weak covalent interactions involving the phenyl ligand are responsible for the observed MO energy shifts in the chain, dimer, and trimer compared to the single BDPA monomer adsorbed on Au(111).

## CONCLUSIONS

In summary, we have demonstrated that BDPA stable radicals form robust clusters up to 300 K on a single-crystal Au support. The radical clusters exhibit a structural richness, which provides a handle for studying geometric and electronic details as well as the radical–radical interaction at the single-molecule level. A different cluster geometry (radical orientation and separation) affects the MO energies by up to 0.6 eV.

Future studies may overcome the high demand on computational power required for a theoretical treatment of the role of the substrate for the radical–radical interaction, which will rely on a comprehensive description of the electronic and geometric properties of the reconstructed Au(111) surface together with the physisorbed radical clusters—exceeding the capabilities of current state-of-the-art methods. The studied BDPA clusters may represent suitable model systems for all-organic quantum spin chains.

## ASSOCIATED CONTENT

### Supporting Information

Details on analyzing BDPA point spectra and complete ref 22. This material is available free of charge via the Internet at <http://pubs.acs.org>.

## AUTHOR INFORMATION

### Corresponding Author

\*E-mail: [stefan.muellegger@jku.at](mailto:stefan.muellegger@jku.at). Phone: +43 732 2468 9624. Fax: +43 732 2468 9696.

### Notes

The authors declare no competing financial interest.

## ACKNOWLEDGMENTS

We thank Wolfgang Jantsch at Johannes Kepler University Linz, Austria, for EPR investigations. We kindly acknowledge

financial support by the Austrian Science Fund (FWF) of the project P20773.

## REFERENCES

- (1) Halliwell, B.; Gutteridge, J. M. C. *Free Radicals in Biology and Medicine*; Oxford University Press: New York, USA, 2007.
- (2) Parsons, A. F. *An Introduction to Free Radical Chemistry*; Blackwell Science Ltd.: London, U.K., 2000.
- (3) Hicks, R. G. *Org. Biomol. Chem.* **2007**, *5*, 1321–1338.
- (4) Gomberg, M. *J. Am. Chem. Soc.* **1900**, *22*, 757–771.
- (5) Gomberg, M. *Ber. Dtsch. Chem. Ges.* **1900**, *33*, 3150–3163.
- (6) Dane, E. L.; Maly, T.; Debelouchina, G. T.; Griffin, R. G.; Swager, T. M. *Org. Lett.* **2009**, *11*, 1871–1874.
- (7) Gatteschi, D.; Sessoli, R.; Villain, J. *Molecular Nanomagnets*; Oxford University Press: New York, USA, 2006.
- (8) Makarova, T. L.; Palacio, F., Eds. *Carbon-Based Magnetism*; Elsevier B. V.: Amsterdam, The Netherlands, 2006.
- (9) Kubo, T.; Katada, Y.; Shimizu, A.; Hirao, Y.; Sato, K.; Takui, T.; Uruichi, M.; Yakushi, K.; Haddon, R. C. *J. Am. Chem. Soc.* **2011**, *133*, 14240–14243.
- (10) Kahn, O. *Molecular Magnetism*; VCH Publishers Inc.: New York, Weinheim, Cambridge, 1993.
- (11) Yazyev, O. V. *Rep. Prog. Phys.* **2010**, *73*, 056501.
- (12) Nygård, J.; Cobden, D. H.; Lindelof, P. E. *Nature* **2000**, *408*, 342–346.
- (13) Narymbetov, B.; Omerzu, A.; Kabanov, V. V.; Tokumoto, M.; Kobayashi, H.; Mihailovic, D. *Nature* **2000**, *407*, 883–885.
- (14) Rajca, A.; Wongsriratanakul, J.; Rajca, S. *Science* **2001**, *294*, 1503–1505.
- (15) McConnell, H. M. *J. Chem. Phys.* **1963**, *39*, 1910.
- (16) Rajca, A. *Chem. Rev.* **1994**, *94*, 871–893.
- (17) Azuma, N.; Ozawa, T.; Yamauchi, J. *Bull. Chem. Soc. Jpn.* **1994**, *67*, 31–38.
- (18) Koelsch, C. F. *J. Am. Chem. Soc.* **1957**, *79*, 4439–4441.
- (19) Duffy, W.; Dubach, J. F.; Pianetta, P. A.; Dekc, J. F.; Strandburg, D. L.; Miedema, A. R. *J. Chem. Phys.* **1972**, *56*, 2555–2561.
- (20) Dalal, N.; Kennedy, D.; McDowell, C. J. *J. Chem. Phys.* **1974**, *61*, 1689–1697.
- (21) Bürgi, L.; Brune, H.; Kern, K. *Phys. Rev. Lett.* **2002**, *89*, 176801.
- (22) Frisch, M. J.; et al. *Gaussian 03*, revision C.02; Gaussian, Inc.: Wallingford, CT, 2004.
- (23) Becke, A. D. *J. Chem. Phys.* **1993**, *98*, 5648.
- (24) Neaton, J.; Hybertsen, M.; Louie, S. *Phys. Rev. Lett.* **2006**, *97*, 216405.
- (25) Thygesen, K. S.; Angel Rubio, A. *Phys. Rev. Lett.* **2009**, *102*, 046802.
- (26) Watanabe, K.; Yamauchi, J.; Ohya-Nishiguchi, H.; Deguchi, Y.; Ishizu, K. *Bull. Inst. Chem. Res., Kyoto Univ.* **1975**, *53*, 161–172.
- (27) Hamilton, W. O.; Pake, G. E. *J. Chem. Phys.* **1963**, *39*, 2694–2697.
- (28) Woll, C.; Chiang, S.; Wilson, R.; Lipple, P. *Phys. Rev. B* **1989**, *39*, 7988–7991.
- (29) Barth, J.; Brune, H.; Ertl, G.; Behm, R. *Phys. Rev. B* **1990**, *42*, 9307–9318.
- (30) Chambliss, D. D.; Wilson, R. J.; Chiang, S. *Phys. Rev. Lett.* **1991**, *66*, 1721–1724.
- (31) Müllegger, S.; Schöfberger, W.; Rashidi, M.; Reith, L. M.; Koch, R. *J. Am. Chem. Soc.* **2009**, *131*, 17740–17741.
- (32) Chen, W.; Madhavan, V.; Jamneala, T.; Crommie, M. F. *Phys. Rev. Lett.* **1998**, *80*, 1469–1472.
- (33) Müllegger, S.; Rashidi, M.; Lengauer, T.; Rauls, E.; Schmidt, W. G.; Knör, G.; Schöfberger, W.; Koch, R. *Phys. Rev. B* **2011**, *83*, 165416.
- (34) Ziegler, M.; Néel, N.; Sperl, A.; Kröger, J.; Berndt, R. *Phys. Rev. B* **2009**, *80*, 125402.
- (35) Müllegger, S.; Rashidi, M.; Fattinger, M.; Koch, R. *J. Am. Chem. Soc.* **2012**.
- (36) Tomba, G.; Stengel, M.; Schneider, W. D.; Baldereschi, A.; De Vita, A. *ACS Nano* **2010**, *4*, 7545–7551.
- (37) Takano, Y.; Taniguchi, T.; Isobe, H.; Kubo, T.; Morita, Y.; Yamamoto, K.; Nakasuji, K.; Takui, T.; Yamaguchi, K. *J. Am. Chem. Soc.* **2002**, *124*, 11122–11130.
- (38) Suzuki, S.; Morita, Y.; Fukui, K.; Sato, K.; Shiomi, D.; Takui, T.; Nakasuji, K. *J. Am. Chem. Soc.* **2006**, *128*, 2530–2531.
- (39) Tian, Y. H.; Kertesz, M. *J. Am. Chem. Soc.* **2010**, *132*, 10648–10649.
- (40) Redhead, P. A. *Vacuum* **1962**, *12*, 203–211.
- (41) Müllegger, S.; Winkler, A. *Surf. Sci.* **2006**, *600*, 1290–1299.